Probing Locally the Onset of Slippage at a Model Multicontact Interface

V. Romero, E. Wandersman, G. Debrégeas, and A. Prevost[*]

Sorbonne Universités, UPMC Univ Paris 06, UMR 8237, Laboratoire Jean Perrin, F-75005 Paris, France
CNRS, UMR 8237, Laboratoire Jean Perrin, F-75005 Paris, France
(Received 7 November 2013; published 4 March 2014)

We report on the multicontact frictional dynamics of model elastomer surfaces rubbed against bare glass slides. The surfaces consist of layers patterned with thousands of spherical caps distributed both spatially and in height, regularly or randomly. Use of spherical asperities yields circular microcontacts whose radii are a direct measure of the contact pressure distribution. Optical tracking of individual contacts provides the in-plane deformations of the tangentially loaded interface, yielding the shear force distribution. We then investigate the stick-slip frictional dynamics of a regular hexagonal array. For all stick phases, slip precursors are evidenced and found to propagate quasistatically, normally to the isopressure contours. A simple quasistatic model relying on the existence of interfacial stress gradients is derived and predicts qualitatively the position of slip precursors.

In recent years, our understanding of the transition from static to dynamic friction has been markedly changed with the development of new imaging techniques to probe spatially the interfacial dynamics at the onset of sliding [1–4]. The transition from the stick to the slip phases was found to involve the propagation of dynamical rupture fronts, far from the Amontons-Coulomb classic picture. Using true contact area imaging with evanescent illumination of a one-dimensional Plexiglas-Plexiglas plane contact, Rubinstein *et al.* [1] measured slow fronts with velocities orders of magnitude lower than the Rayleigh wave velocity v_R, along with sub-Rayleigh and fast intersonic fronts. Up to the macroscopic slippage, these fronts progressively invade the contact over a length $l(t)$ from the trailing edge [2]. Interestingly, using strain gauges sensors distributed directly above the interfacial plane, the same group reported strong correlations between $l(t)$ and the ratio of tangential to normal local stresses [5]. However, in all these experiments, the contact was treated as a one-dimensional interface. For a two-dimensional contact, simultaneous measurements of both pressure and tangential interfacial fields is still lacking and out of reach using Ben-David and Fineberg's approach. It also remains unclear what physical mechanism sets the dynamics of $l(t)$ and slip fronts direction of propagation, despite numerous theoretical as well as numerical works [6–10].

In this Letter, we take advantage of recent developments in micromilling techniques to design model elastomer multicontact surfaces. These consist of thousands of spherical caps distributed on top of a rectangular block, all made from the same elastomer. We show that spherical caps provide a unique way to measure optically local normal and shear forces once in contact with bare glass slides. We apply this novel technique to analyze the stick-slip frictional dynamics of an hexagonal array of spherical caps of equal height and radius of curvature. Local analysis first reveals that pressure gradients are inherently present for this plane-plane contact, and second that each stick-slip event is mediated by slip precursors. These are found to be quasistatic and to propagate normally to the isopressure lines. We compare our findings with a simplified pressure gradient based model where individual asperities are taken as elastically independent.

Microstructured surfaces are obtained by pouring and curing (see Ref. [11] for details) a PolyDimethylSiloxane (PDMS Sylgard 184, Dow Corning) in a Plexiglas mold fabricated with a desktop CNC Mini-Mill machine (Minitech Machinary Corp., USA). The molds consist of 10×10 mm^2 square cavities, 2.5 mm deep. Their bottom surface is covered with spherical holes whose constant radius of curvature $R = 100$ μm is set by the ball miller used. Holes are positioned spatially with 1 μm resolution either over a regular lattice or at random and their maximum depths are either equal or taken at random from a uniform distribution in the range 40–60 μm. Resulting PDMS surfaces are decorated with spherical caps which match the designed pattern. For the present work, different types of patterns were fabricated–two hexagonal lattices with a base surface coverage $\Phi = 0.4$, one with constant height asperities (LC) and one with random height asperities (LR), and two random distributions with random height asperities (RR), with $\Phi = 0.2$ and 0.4. Samples are maintained by adhesion against a solid glass plate, cleaned with isopropanol then dried, and put in contact with a clean bare glass slide under constant normal load P. The glass slide is mounted on a double cantilever system (see Supplemental Material [12] and [11]) which allows us to measure both P and the applied shear force Q with mN resolution in the range [0–2.5] N. All experiments are performed at room temperature. The glass slide can be

driven at constant velocity v in the range [4–1000] μm/s along the x direction. The interface is imaged in transmission with an LED array through the glass slide, with a megapixel CMOS sensor based camera (Photon Focus, 130 Hz) or a fast camera (Photron Fastcam APX-RS, 1000 Hz). As shown on Fig. 1(a), light is transmitted at every single microcontact and refracted by the spherical caps elsewhere, resulting in a myriad of white circular spots, whose radii a_i can be extracted using image analysis [Fig. 1(a), inset]. Assuming Hertz's model to describe the glass-spherical cap contact, the local applied load p_i is given by

$$p_i = \frac{4Ea_i^3}{3(1-\nu^2)R}, \tag{1}$$

where E is the elastomer Young's modulus and $\nu = 0.5$ [11] its Poisson's ratio. This allows computing the total normal load $P_c = \sum_i p_i$. For all experiments, a linear relationship is systematically found between P_c and P over 2 orders of magnitude in P, irrespective of the type of disorder and pressure distributions [Fig. 1(b)]. Hertz assumption is thus clearly validated in normal contact conditions. However, the slope of P_c versus P depends slightly on the optical threshold used to detect a_i. To recover a unit slope, we thus calibrated the optical threshold with a reference sample whose Young's modulus $E = 4.1 \pm 0.1$ MPa has been measured independently with a JKR test [13]. We then kept the resulting threshold for other samples and tuned E within experimental errors to recover a unit slope. Upon shearing the interface, obtained by driving the translation stage at constant v in the range [20–120] μm/s, the microcontacts size changes marginally from circular to slightly elliptic, still allowing p_i to be extracted within Hertz assumption.

Contrary to the usual pillar geometry of asperities [14–16], spherical asperities do not bend nor buckle. It is thus possible to locate unambiguously with sub-pixel accuracy (1/24 pixels, ~400 nm) positions of the microcontacts centers and follow, using a custom made algorithm written in MATLAB (MathWorks), their displacements with respect to their initial position, u_c [Fig. 1(c), upper panel]. The same methods allow us to extract the displacement of the back layer by monitoring positions of the base of spherical asperities, u_b [Fig. 1(c), lower panel]. Defining $\delta = u_c - u_b$ as the displacement of the cap top with respect to the back layer, we measured $\delta \approx \alpha vt$ with $\alpha \approx 0.032$ for the LC pattern. Neglecting any microslip at the edges of the microcontacts [11], the local shear force q_i is proportional to a_i [13], according to

$$q_i = \frac{8Ea_i}{3(2-\nu)}\delta. \tag{2}$$

The total shear force Q_c is obtained writing that $Q_c = \sum_i q_i$. For all patterns, Eq. (2) provides a good approximation for the local shear force as shown on Fig. 1(d). A one-to-one linear relationship between Q_c and Q over 2 orders of magnitude is found. The inset of Fig. 1(d) illustrates this agreement with $Q(t)$ and $Q_c(t)$.

We now turn onto analyzing in details the frictional dynamics of the LC pattern, the simplest available texture, sheared along x. Q is found to increase up to a static threshold, beyond which a stick-slip instability always sets for all P and v within [20 μm/s–120 μm/s] [Fig. 1(d), inset]. In the stick-slip regime, the spatial distribution of local normal forces is found to be nonuniform with a characteristic saddle-like shape [Fig. 2(a)] and is time invariant. Such nonuniformity presumably results from combined effects of a curvature of the PDMS sample at long wavelengths, contact loading configuration and history [5] and Poisson expansion [14]. Analysis of the displacement curves $u_c(t)$ reveals that during initial and subsequent stick phases, slip precursors nucleate and eventually invade the whole contact. In the stick-slip regime, they can be best evidenced when looking at two-dimensional velocity field
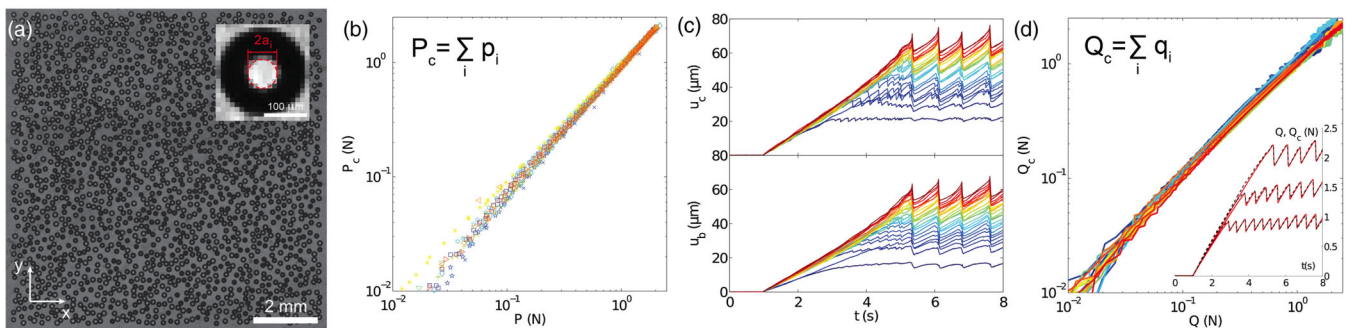

FIG. 1 (color online).   (a) Contact image of a RR sample ($\Phi = 0.4$, $P = 2$ N). Inset: single asperity in contact (contact diameter $2a_i$). (b) P_c versus P for all patterns (different colored symbols) loaded normally. (c) Microcontact (back layer) displacements $u_c(t)$ [$u_b(t)$] for 23 microcontacts chosen at random in the LC sample ($v = 80$ μm/s, $P = 2$ N). p_i increases from bottom to top (blue to red). (d) Q_c versus Q for all patterns (different colored lines) in shear experiments. Inset: $Q(t)$ (solid lines) and $Q_c(t)$ (dashed lines) for the LC pattern with $P = 0.5$, 1, 2 N (bottom to top) and $v = 80$ μm/s.
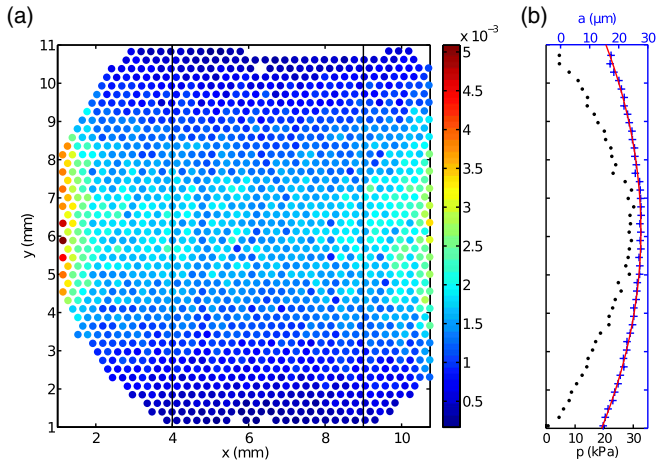
FIG. 2 (color online). (a) Spatial distribution of normal local forces (in N) for the LC pattern in the stick-slip regime ($P = 2.36$ N, $v = 50$ μm/s). (b) Pressure (filled circle) and radii (plus sign) distributions averaged along x in the region bounded by the two vertical lines in (a). The line is a fit $a(y) = a_0 + a_1 y + a_2 y^2$ with $\{a_0, a_1, a_2\} = \{8.37$ μm, 6.27 10^{-3}, -0.51 m$^{-1}\}$.

snapshots du_c/dt [Figs. 3(a)–3(c)] at three instants shown on Fig. 3(d) (see Supplemental Material [12]). In the stick phase ($t \leq t_s$, where t_s is the time of slip, different for each event), they appear as spatially localized structures with large negative velocities, indicative of a collective backsnapping of the microcontacts [Figs. 3(a)–3(c)]. A secondary slip pulse also forms several asperities behind the first one [Figs. 3(b)–3(c)]. These two consecutive slip pulses are systematically observed
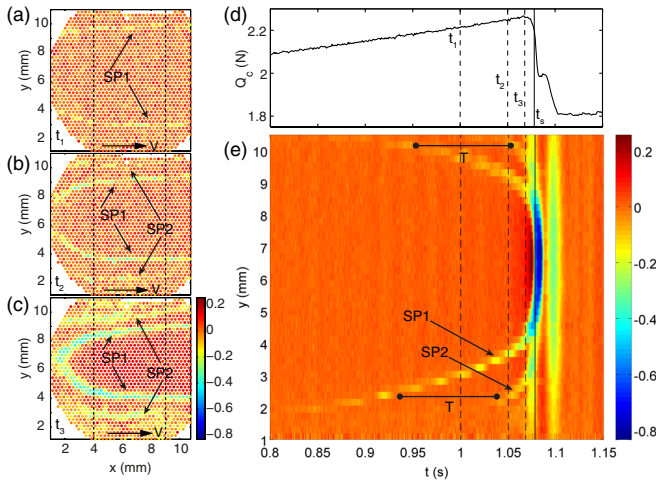

FIG. 3 (color online). (a)–(c) Velocity field snapshots, obtained at 1000 Hz, at times t_1 (a), t_2 (b), and t_3 (c). SP1 (SP2) stands for 1st (2nd) slip pulse. The black arrow shows the direction of sliding. Vertical lines delimit the region defined in Fig. 2(a). ($P = 2.36$ N, $v = 50$ μm/s) (d) $Q_c(t)$ for the stick-slip event of (a)–(c). Dashed lines are drawn at times t_1, t_2, and t_3. (e) Spatiotemporal plot of the velocity field along y averaged for $4 \leq x \leq 9$ mm. Velocities are given in mm/s. T is the delay between SP1 and SP2.

for all stick-slip events, and always nucleate on the contact edges. When focusing on the central band $4 \leq x \leq 9$ mm, front lines are essentially oriented along x normally to the isopressure lines (see Figs. 3(a)–3(c) [17]). Within this band, the velocity field along the y direction is averaged over x to help visualizing how the front propagates spatially over time.

On the resulting spatiotemporal plot [Fig. 3(e)], both first and second slip pulses are visible, each of them consisting of two branches, almost symmetric with respect to the $y \approx 6$ mm axis. The first slip pulse appears to propagate initially with a constant velocity before continuously accelerating as t approaches t_s, reaching a maximum velocity of about 0.5 m/s, 2 orders of magnitude lower than v_R (≈ 30 m/s for PDMS). The observed scenario remains qualitatively similar for the first loading stick phase, but slip precursors are more heterogeneously distributed, preventing a direct quantitative analysis. This difference is likely related to slight pressure distribution rearrangements during the first loading phase. For the present work, we have thus chosen to focus on the stick-slip regime only.

For each stick-slip event, front positions were obtained by detecting individual times of slip for each asperity in contact, using their displacement $u_c(t)$, allowing us to obtain them with a better accuracy. Mean front positions versus mean times of slip were deduced by averaging both individual slip times of all asperities at the same y position (within the central x band) and mean front positions on all stick-slip events. Similarly to the velocity spatiotemporal representation, such curves are almost axisymmetric around $y \approx 6$ mm, allowing us to extract the distance c to this axis of symmetry, which is a direct measure of the remaining stick zone extension. This procedure was applied for 6 experiments at $P = 2.36$ N with increasing driving velocities v. Figure 4 shows the resulting c versus $(t_s - t)$ for the first slip pulse [Fig. 4(a)] and the same data with the time axis multiplied by v [Fig. 4(b)]. All curves at different v are found to overlap on the same master curve, suggesting that propagation of slip precursors results from a quasistatic
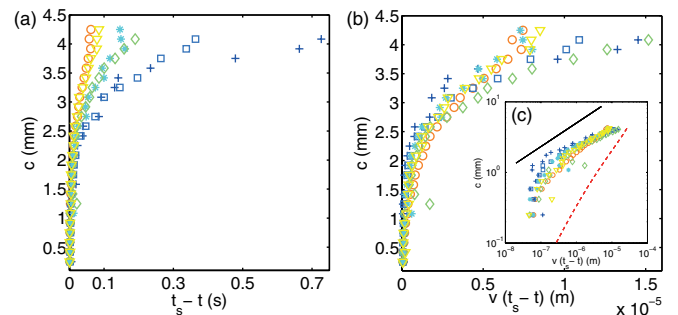

FIG. 4 (color online). (a) c versus $(t_s - t)$ for the first slip pulse and $v = 20$(plus sign), 30(square), 50(diamond), 80(asterisk), 100(triangle), 120(circle) μm/s. (b) c versus $v(t_s - t)$. (c) Log-log plot of (b). The solid line is a power law of exponent $1/3$. The dashed line is the model prediction.

mechanism. Note that these curves do not include any data at $t > t_s$ in the slip phase. For $t > t_s$, a fast front which can be seen as the second vertical yellow line on Fig. 3(e), propagates from the center to the edges with a velocity larger than 2–3 m/s. This front whose nature is possibly inertial is not further studied here.

On the experimental side, our measure of $c(t)$ is analogous to that of $L - l(t)$ of [2,5], with L being the size of the system. Our work provides two additional features of these slip fonts: (i) their quasistatic nature; (ii) the way the two-dimensional pressure landscape controls their propagation, as discussed below. On the theoretical [9,18,19] and numerical [7,8] sides, recent investigations have predicted similar quasistatic behaviors for the slip front position $l(t)$, and its relation to the stress landscape [7], L and local friction laws [8,9,18,19]. In particular, [9,18,19] assume rate and state interfacial friction laws, and predict the existence of a critical length l_c beyond which the system becomes unstable. For $l < l_c$, slip fronts are found to be quasistatic [18,19], but the precise analytical form of $l(t)$ is not well established. For $l > l_c$, a dynamic front invades the interface with a velocity $\sim v_R$, leading to macroscopic slippage. The slight change of slope of $c(t)$ observed at $t \sim t_s$ [Fig. 4(c)] could be a signature of such a transition, as in [2]. However, front velocities at $t \sim t_s$ (Fig. 4) appear to be 2 orders of magnitude smaller than v_R, ruling out inertia as the driving mechanism.

To understand the form and quasistatic nature of $c(t)$, let us model our system with asperities distributed along y (the direction normal to the isopressure lines) on a one-dimensional regular lattice, and let us neglect the elastic interaction between them (i.e., absence of any back layer). In the Amontons-Coulomb description, slip of an asperity i occurs once $q_i = \mu_s p_i$, where μ_s is a static friction coefficient. Combining Eqs. (1) and (2) yields the maximum displacement δ_s^i, beyond which slip occurs, as

$$\delta_s^i = \mu_s a_i^2 / R. \qquad (3)$$

An asperity i initially at position y_0^i will slip when its position reaches $y_s^i = y_0^i + \delta_s^i \approx y_0^i$, since $\delta_s^i \ll y_0^i$. With Eq. (3), the front position and time of slip, respectively $y_w = y_s^i$ and $t_s^i = \delta_s^i / (\alpha v)$, are thus predicted for a given pressure profile. In an ideal plane-plane contact with a uniform pressure, all asperities should slip simultaneously and no slip pulse should be observed. In our experiments, however, pressure gradients are clearly present along y [Fig. 2(a)]. Taking a continuous limit, the contact radius a_i can be well fitted by a parabola $a(y) = a_0 + a_1 y + a_2 y^2$ [Fig. 2(b)]. This expression, with Eq. (3), provides the position of the front with respect to its position at threshold, $c(\delta) = y_w(\delta_s) - y_w(\delta)$, where $\delta_s = (\mu_s/R)(a_0 - (a_1^2/4a_2))^2$ is the threshold displacement at $t = t_s$. It reads

$$c(\delta) = -\frac{1}{2a_2}(a_1^2 - 4a_2(a_0 - (R\delta/\mu_s)^{1/2}))^{1/2}. \qquad (4)$$

This quasistatic model can be extended to any pressure distribution and provides a description of the first loading phase, where all microspheres start from their initial unloaded position. Once a sphere slips, it relaxes back from δ_s^i by $\delta_r^i = (\Delta\mu/\mu_s)\delta_s^i$ before the beginning of a next loading phase, where $\Delta\mu = \mu_s - \mu_d$ with μ_d a dynamical friction coefficient. The model can be extended to the stick-slip events by replacing μ_s by $\Delta\mu$ in Eq. (4). Note that close to the threshold ($\delta - \delta_s \ll \delta_s$), $c(\delta)$ behaves asymptotically as $c(\delta) = K(\delta_s - \delta)^{1/2}$ with $K = (2R/(\Delta\mu(a_1^2 - 4a_0a_2)))^{1/2}$. One thus expects $c(\delta)$ to follow a power law of exponent $1/2$. Predictions of Eq. (4) are plotted on Fig. 4(c), with $\{a_0, a_1, a_2\}$ given by the parabolic fit [see caption of Fig. 2(b)] and $\Delta\mu = 0.157$, obtained by averaging values of $\Delta\mu$ for all experiments. The predicted curve qualitatively succeeds in reproducing the measured trend and right order of magnitude of $c(\delta)$, but fails quantitatively. Careful examination of the data suggests that c follows indeed a power law, but with an exponent closer to $1/3$ than $1/2$ [Fig. 4(c)]. Our model lacks ingredients which could explain the discrepancies. First, it is limited to a one-dimensional description, whereas the slip propagation is clearly two dimensional. Second, it does not take into account the elastic coupling between asperities. Including both effects is expected to improve comparison, but is beyond the scope of this Letter.

Despite its limitations, this model provides a simple mechanism to generate slip pulses, relying on interfacial stress gradients. Interestingly, it also predicts the existence of second slip pulses whose propagation is delayed by T, as evidenced on Fig. 3(e). T results from the sum of (i) the individual relaxation time τ of a sphere sliding back from δ_s^i by δ_r^i, and (ii) the time to reach δ_s^i again, yielding $T = \tau + \delta_r^i / (\alpha v)$. Such relationship is actually verified experimentally (not shown), asserting furthermore the quasistatic character of the measured slip pulses. Taking $\tau = 7.6 \pm 0.5$ ms, the averaged relaxation time over all trajectories, one gets $\delta_r^i \approx 0.35$ μm, comparable to the measured averaged value of 1 μm. In addition, the second slip pulse can only be identified if $T(i = 0) < t_s$. This gives a limiting driving velocity v_l above which no second slip pulse can be observed, $v_l = \frac{1}{\tau}(\delta_r - \delta_r^{i=0}) = \frac{\Delta\mu}{\alpha R\tau}((4a_2a_0 - a_1^2/4a_2)^2 - a_0^2)$. Using the experimental values, one gets $v_l \approx 4.4$ mm/s, much larger than the maximum tested driving velocity. This agrees with a systematic observation of a second slip pulse at all velocities.

This work has been limited to the stick-slip regime, where slip fronts could be characterized and compared to a noninteracting model. A similar phenomenology is observed for the first stick event, and will be explored in a future work. Our results demonstrate how combining surface micropatterning and interface imaging allows

accessing the mechanics at the level of single asperities. This has been applied to a hexagonal array of equal height microasperities, revealing that slip precursors propagate quasistatically orthogonally to the isopressure lines. It will be extended to more elaborate patterns in a future work.

———————

[*]alexis.prevost@upmc.fr

[1] S. M. Rubinstein and G. Fineberg, Nature (London) **430**, 1005 (2004).

[2] S. M. Rubinstein, G. Cohen, and J. Fineberg, Phys. Rev. Lett. **98**, 226103 (2007).

[3] O. Ben-David, S. M. Rubinstein, and J. Fineberg, Nature (London) **463**, 76 (2010).

[4] M. C. Audry, C. Fretigny, A. Chateauminois, J. Teissere, and E. Barthel, Eur. Phys. J. E **35**:83 (2012).

[5] O. Ben-David and J. Fineberg, Phys. Rev. Lett. **106**, 254301 (2011).

[6] O. M. Braun, I. Barel, and M. Urbakh, Phys. Rev. Lett. **103**, 194301 (2009).

[7] J. Scheibert and D. K. Dysthe, Europhys. Lett. **92**, 54001 (2010).

[8] J. Trømborg, J. Scheibert, D. S. Amundsen, K. Thogersen, and A. Malthe-Sorenssen, Phys. Rev. Lett. **107**, 074301 (2011).

[9] E. Bouchbinder, E. A. Brener, I. Barel, and M. Urbakh, Phys. Rev. Lett. **107**, 235501 (2011).

[10] D. S. Amundsen, J. Scheibert, K. Thøgersen, J. Trømborg, and A. Malthe-Sørenssen, Tribol. Lett. **45**, 357 (2012).

[11] A. Prevost, J. Scheibert, and G. Debrégeas, Eur. Phys. J. E **36**, 17 (2013).

[12] See Supplemental Material at http://link.aps.org/supplemental/10.1103/PhysRevLett.112.094301 for a sketch of the experimental setup and a movie of the two-dimensional velocity field during the stick-slip event of Fig. 3.

[13] K. L. Johnson, Contact Mechanics (Cambridge University Press, New York, 2003).

[14] K. Brörmann, I. Barel, M. Urbakh, and R. Bennewitz, Tribol. Lett. **50**, 3 (2013).

[15] B. Murarash, Y. Itovich, and M. Varenberg, Soft Matter **7**, 5553 (2011).

[16] E. Degrandi-Contraires, C. Poulard, F. Restagno, and L. Léger, Faraday Discuss. **156**, 255 (2012).

[17] This observation was reproduced with samples with the same hexagonal pattern but a different pressure distribution.

[18] M. Otsuki and H. Matsukawa, Sci. Rep. **3**, 1586 (2013).

[19] Y. Bar-Sinai, R. Spatschek, E. A. Brener, and E. Bouchbinder, Phys. Rev. E **88**, 060403(R) (2013).